Experimental study and model simulation of spinodal decomposition in a binary mixture under shear

C. K. Chan,* F. Perrot, and D. Beysens
Service de Physique du Solide et de Résonance Magnétique, Institut de Recherche Fondamentale, Commissariat à l'Energie Atomique, Centre d'Etudes Nucléaire Saclay, 91191 Gif-sur-Yvette CEDEX, France
(Received 9 August 1989; revised manuscript received 17 September 1990)

We report results of a detailed study by light scattering and a model simulation of spinodal decomposition in a binary liquid mixture under constant uniform shear flow. The effects of flow are found to be important when the growth rate of the phase-separating domains is smaller than the shear rate. The growth of these domains is strongly modified by the shear flow only in certain directions. In the direction perpendicular both to the flow and shear, the flow has little effect on the growth. Some essential features observed in the experiments are reproduced in a computer simulation that incorporates only the deformation produced by the flow. The effect of surface tension must be considered to account for the other observed effects. A new growth mechanism can be induced by the interaction of capillary forces with the shear flow.

I. INTRODUCTION

It is well known that dynamics of the growth of phase-separating domains are influenced by the hydrodynamics of the system.[1] One might expect that the dynamics of growth would be altered when the hydrodynamic interactions between the phase-separating domains are modified, for example, by an externally imposed flow. In fact, it has been observed in fluid systems that flows driven by gravity[2,3] accelerate and modify the phase-separating process and thus novel growth mechanisms might be present. In this article we present experimental and simulation studies of the dynamics of growth for a critical binary liquid mixture undergoing spinodal decomposition (SD) in the presence of a uniform shear flow.

When a binary liquid mixture close to the critical point is subject to a shear flow of shear rate S, there are at least two associated relevant time scales: the characteristic time τ of the critical fluctuations[4] and the time scale S^{-1} of the shear flow. Depending on the value of the product $S\tau$, two regimes can be defined, namely $S\tau > 1$ and $S\tau < 1$. For the case of $S\tau > 1$ or "strong-shear" regime, the critical fluctuations are strongly modified by the flow while for the case $S\tau < 1$ or "weak-shear" regime, the critical fluctuations are slightly affected.[5] Figure 1 shows schematically these two regions in the phase diagram (concentration c, temperature T).

For the strong-shear case in the one-phase regime, there have been a number of theoretical and experimental studies.[5] In general, the agreement between theory and experiment is satisfactory. The main results are that the critical fluctuations are strongly anisotropic, the critical exponents assume mean-field values, and the critical temperature is shifted downward by the shear.

In contrast, not much attention has been paid to the case $S\tau < 1$, because critical phenomena are not affected by the flow. Note that the regime of $S\tau < 1$ exists both above and below T_c (respectively I and II in Fig. 1). Even though these two regions I and II are both in the regime of $S\tau < 1$, they are fundamentally very different. In regime I, there is no thermodynamic instability for a homogeneous fluid. Nevertheless, above T_c, the slight anisotropy of critical fluctuations leads to a very large birefrigence and dichroism.[6] However, a homogeneous fluid in regime II will be unstable and a phase separation will occur. Intuitively, since the critical properties of the system are slightly affected by the flow in this regime, phase separation should proceed as if there were no shear flow

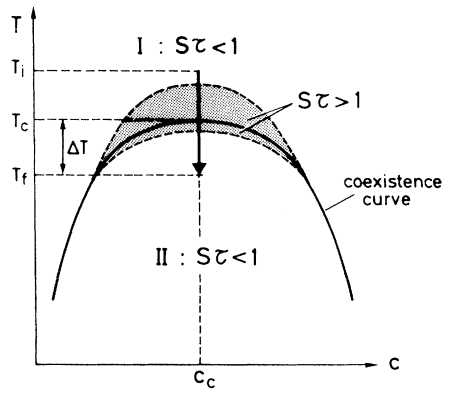

FIG. 1. Phase diagram of a binary mixture under a uniform shear slow (shear rate S). The hatched region on both sides of the coexistence curve corresponds to the strong shear regime. Region I (above the coexistence curve) and region II (under the coexistence curve) correspond to the weak-shear regime (see text). A typical thermal quench performed in the experiment is represented: the system is quenched from the temperature T_i in the region I to the temperature T_f in region II. Typically, $T_i - T_c \simeq 2$ to 5 mK and $T_c - T_f \simeq 0.5$ to 5 mK.

and sharp interfaces will be formed. But, once these domains begin to grow, another time scale enters the problem; namely, the growth rate of the domains. If this later time scale is smaller than that of the flow, we expect that growth will be modified by the flow and a new growth mechanism can be induced.

In order to study the interaction between flow and domain growth in the regime $S\tau < 1$, we have performed light-scattering experiments on spinodal decomposition of a binary mixture under a constant uniform shear flow and preliminary results have been reported previously.[7–9] We found that growth of the phase-separating domains is strongly modified by the shear flow only in certain directions. In the direction perpendicular to the flow and the shear, shear seems to have little effect on the growth. Since few theoretical calculations on SD under shear[10–12] have been performed to date and since we have only one for comparison,[12] a simple simulation has been carried out to explain our data. In this simulation, only the deformation effect of the shear flow on an interconnected SD-like structure has been considered and surface tension is neglected. In this model we have also assumed that the shear rate is much larger than the growth rate of the domains and that there is no growth mechanism. Even in such a simple model we find that some of the essential features of the experiments are reproduced. However, surface tension must be included to explain some of our observations, which indicate that a new growth mechanism is induced by interaction of surface tension with the flow.

In Sec. II we describe the apparatus and the experimetnal method. The main difficulties of the design and calibration procedure are discussed. The results of the experiment are then presented in Sec. III. In Sec. IV, the simulation and its results are presented. Here we show that the deformation effect of the flow is important. The discussions of our results and their interpretation and given in Sec. V and concluding remarks are given in Sec. VI.

II. LIGHT-SCATTERING EXPERIMENT

Our experiment is similar to other light-scattering experiments on binary mixtures in that the sample is brought suddenly (quenched) from a temperature T_i above the critical temperature T_c to a temperature T_f below T_c (see Fig. 1), while the small angle scattered intensity is recorded. The difference here is that there is a shear flow inside our sample. Since we are studying an anisotropic phenomenon, two light beams are used at orthogonal directions. This aspect of our experiment is very different from traditional experiments where only a single beam is used. One of the difficulties of a well-controlled flow experiment with binary liquid mixture is the design and fabrication of the sample cell. We will give details of such a cell. As we will show below, contamination is inevitable in such a cell. Special care has been taken to measure the critical temperature and the method will be discussed.

A. The Couette device

In order to generate a reasonably uniform and permanent shear flow, a Couette device is used in the experiment. Since the light-scattering experiment concerns a binary mixture, it is necessary that the cell must be transparent and sealed. Figure 2 shows the details of the essential parts of the apparatus. The Couette device consists of three pieces of glass; an outer cylinder (G_1), a movable cylinder (G_2), and a piece (G_3) which holds the rotation support (RG) and seals the Couette with the outer cylinder. The RG is made of stainless steel and has two internal ball bearings without lubricant. The movable cylinder is fixed to G_3 through a stainless-steel bar (SB) that runs through RG and has the movable cylinder (G_2) and a magnet (M) attached to each of its ends by stainless-steel nuts. The different parts of the cell are held together by a stainless-steel housing also shown in Fig. 2. The cell is sealed by using indium o-rings between the glass surfaces (G_1 and G_3) and stainless-steel surfaces. These are two small holes in RG and the housing to allow filling of the sample. The holes in the housing are sealed by using a screw and indium ring after the sample has been filled.

With this design, we in fact have two Couette flows in one cell, namely, the gap between the inner wall and the moving cylinder and that of the outer wall and the moving cylinder. The two Couette flows correspond to a moving inner cylinder device and a moving outer cylinder device, respectively. It is well known that there is a hydrodynamic instability (Taylor-Couette) in moving inner cylinder devices when the rotational speed exceeds a critical value.[13] However, in the experiments reported below, the rotation speed is so low that we are always far from this hydrodynamic instability in the outer cell. With the radii of the inside surfaces of the walls of G_1:22 and 26.5 mm and those of the moving cylinder: 23.5 and 25 mm, the shear rates produced in the inner and outer cells are 1.64ω sec^{-1} and 1.75ω sec^{-1}, respectively,

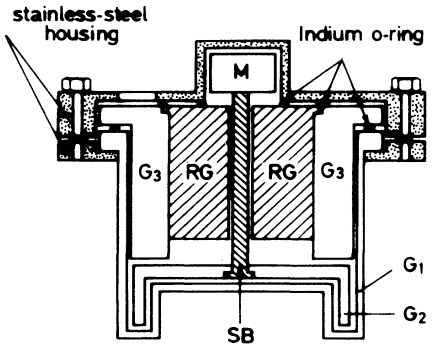

FIG. 2. The Couette device showing the glass parts (G_1, G_2, G_3) and the stainless-steel parts (RG, SB). (See text for the letter symbols.)

where ω is the angular velocity of the rotating cylinder in revolutions per minute (rpm).

B. Sample preparation and calibration

Before the Couette device is assembled, all the glass parts were cleaned with sulfochromic acid while the stainless-steel parts and the ball bearings were cleaned with acetone and alcohol. After assemblage, the cell is filled with a critical mixture of water and isobutyric acid prepared after weighing. The weight percentage of the mixture used is 61% of water that is taken from reported values.[14] After the cell has been placed under water in the bath to be described below, criticality of the mixture is checked by measuring the turbidity in the homogeneous phase. The critical temperature T_c of our sample immediately after filling is 26.7 °C, which is slightly higher than the reported value of 26.2 °C.[14] However, it is well known that the critical temperature of a binary mixture is sensitive to impurities while its critical properties are only little affected.[15]

During the course of the experiment, there is a downward drift of T_c. This was about 5 mK per day with no rotation in the Couette device. However, when it was rotating rapidly, a 1-mK shift in T_c has been measured in less than an hour, which is the order of magnitude of the duration of an experiment. The drift of T_c depends on how often the cell is turned. Our explanation for these observations is that there is a slow chemical reaction of the stainless steel, indium ring, and especially the bearings with the mixture and therefore contaminants are produced which enter into the bulk during rotation. In fact, at the end of the lifetime of our sample, which is about five to six weeks, the color of the sample has changed from clear to yellowish brown. Three different samples (fillings) have been used in these experiments.

Because of the drift of T_c, a special method is devised to measure T_c during the experiment. For each quench experiment with shear, two quench experiments without shear but the same quench depth are also performed, one before and one after the shear quench. We then use these two no-shear experiments to determine their T_c by comparing them to previously calibrated quench experiments. The criterion is that if the T_c determined from these no-shear experiments agree with each other, we can safely assume that the T_c for the shear experiments is the same. Otherwise, the shear experiment is rejected since T_c cannot be assigned.

C. Setup

After the sample has been filled and sealed, it is mounted on a waterproof support which provides a rotation mechanism to drive the movable cylinder inside the cell by magnetic coupling. An electric motor and a gear box are also mounted on the same support to provide rotation at different speeds from 0.01 to 1 rpm. This support, with the cell mounted, is fixed on the top of a water bath (Fig. 3), so that the cell is well under water. A He-Ne laser is also on the top of the bath with the beam directed

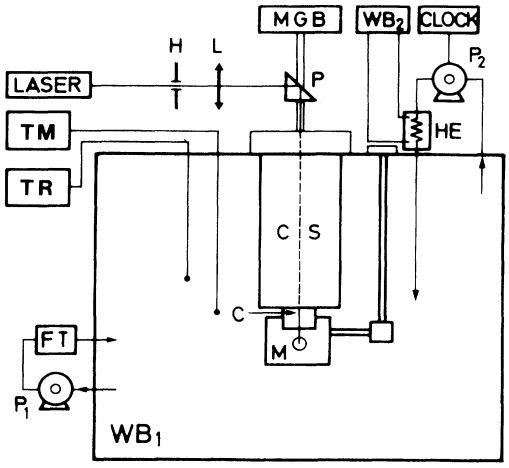

FIG. 3. Setup of the experiment showing only the laser beam of direction A. H, pinhole; L, lens; P, prism, C, Couette device, CS, Couette support; M, mirror, MGB, motor and gear box; WB_1, WB_2, temperature regulated water baths; P_1, P_2, pumps, HE, heat exchanger; FT, water filter; TR, thermal regulation; TM, temperature measurement.

through the gap of the sample by a prism. Before the beam strikes the prism, it is cleaned by a pin hole with a diameter of 1 mm and slightly focused by a lens of 50 cm focal length. Since the laser beam is Gaussian, this corresponds to a collimation. The lens is mounted on an x-y translation stage so that the position of the beam in the sample can be tuned. The beam can be directed to go through either the inner or the outer cell. There is a mirror mounted inside the water bath to reflect the laser beam horizontally (Fig. 4). Another laser beam is directed through the sample in a direction perpendicular to the first one by this mirror and a small mirror glued to the cell (Fig. 4). Thus there are two beams traversing the sample at right angle to each other. We will call the beam which is parallel to the walls of the cell beam A and the direction defined by it as direction A. Similarly beam B and direction B refer to the other beam. Notice that direction A is perpendicular to the flow and the shear while direction B is also perpendicular to the flow but it is parallel to the shear. Figure 4(a) shows the geometry of the scattering.

The temperature of the bath is controlled by a digital temperature controller[16] to within ± 0.2 mK over a few days. The quench of the sample is carried out by cooling the bath quickly by means of a heat exchanger working for a calibrated time period. However, there is a time lag between the temperature of the bath and the temperature inside the sample. The calibration of a quench is carried out by monitoring the transmittance of the laser beam which is sensitive to the temperature of the sample when the sample is just above the critical point.[17] Typically, for a 5-mK quench, the quench takes about 20 sec.

We are interested in how the scattered intensities depend on the strength of the shear and the depth of the quench. To detect the scattered intensity, a screen made

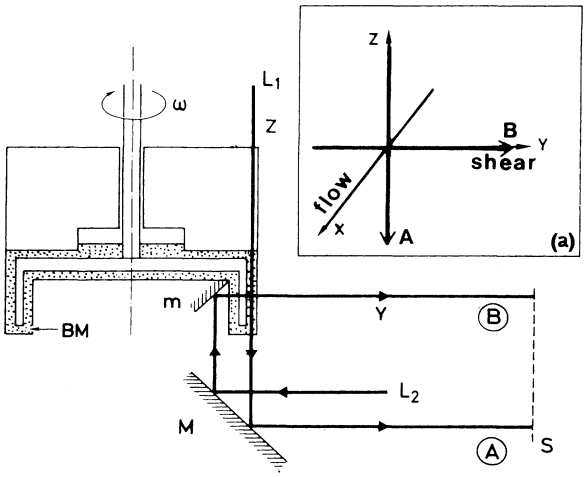

FIG. 4. Light paths of the two directions A and B. L_1, L_2, He-Ne lasers; m, M, mirrors, S, screen; BM, binary mixture; ω, angular velocity of the rotating cylinder. In (a), the two directions A and B are drawn with respect to the axes x (flow direction), y (shear direction) and z (rotation axis).

of tracing paper is placed 50 cm away from the bath with its plane perpendicular to the two beams (A and B) coming out of the bath after traversing the sample (Fig. 4). The light-scattering pattern falling on this screen is detected by a video camera and stored in a video recorder for later analysis. During a typical experiment, the sample is first kept in a steady state at a temperature T_i above T_c with the shear applied and then the temperature is quenched to T_f below T_c while scattered intensities falling on the screen are recorded.

As is clear from Fig. 4 the optical paths in the sample in direction A and B are different. The effect of multiple scattering is more important in direction A. Furthermore, because of the cylindrical surface of the cell in direction B, the scattering patterns are slightly distorted in the k_x direction and a correction factor is needed. This correction factor is obtained by examining quenches without shear where the scattering pattern should be a ring. Finally, in direction B, there are actually two Couette cells in the path with a 6% difference in shear rate and the directions of shear in these two cells are antiparallel. As will be seen below, the scattering pattern in this direction is symmetric about the k_z and k_y axes and therefore the different directions of shear in these two cells do not create any difficulty.

III. RESULTS OF EXPERIMENTS

In this section we only report the results of our experiment. The discussion and interpretation will be deferred to Sec. V after presentation of the simulation results.

First, we recall some useful quantities for the water and isobutyric acid mixture:[14] correlation length $\xi^- = \xi^+/2 = 1.8|\epsilon|^{-\nu}$ (Å) with ξ^- (ξ^+) for the correlation length in the two-phase region (one-phase region), $\nu = 0.63$ and ϵ the reduced temperature $\epsilon = (T_c - T)/T_c$, viscosity $\eta = 0.025$ (cgs units) and surface tension σ: $\sigma = \sigma_0 \epsilon^{\mu}$ with $\mu = 2\nu$ and $\sigma_0 = 12$ dyn cm^{-2}. The typical lifetime of critical fluctuations is given by $\tau^- = 6\pi\eta(\xi^-)^3/k_B T_c$, where k_B is the Boltzmann constant.

Although we could perform our experiment in the two directions simultaneously, we usually performed our experiment in one direction at a time to avoid stray light and overlapping of scattering patterns. Furthermore, the effects of multiple scattering in these two directions are also different. Therefore we will present our quantitative results in the two directions separately. However, in order to compare the behavior in the two directions at the same time, scattering experiments with directions A and B simultaneously are also reported. Note that in all the experiments, the system is always in the regime of weak shear, i.e., $S\tau < 1$ and we always use the outer cell in direction A. Since we are using a video camera to collect data, we do not have very good intensity resolution (two decades); however, the spatial resolution is adequate. In the following we will discuss only the spatial information.

A. The phenomenon

Figure 5 shows the scattering pattern at different times after the quench for direction A [Fig. 5(b)] and direction B [Fig. 5(c)] during the phase separation together with the definition of the scattering axes. The case without shear [Fig. 5(a)] is also shown here for comparison. In these figures, the quench depth is $\Delta T = T_c - T_f \simeq 1.5$ mK. The shear rate is 0 for Fig. 5(a) and 0.035 sec^{-1} for both Fig. 5(b) and Fig. 5(c). It can be seen that the maxima of the scattered intensities in both directions [Figs. 5(b) and 5(c)] are deformed by the flow from the form of a ring into the form of an ellipse. In both directions, we are interested in the size and shape of these ellipses, which provide information about the size and the shape of the phase-separating domains. There are three parameters for an ellipse: the length of its major axis, the length of the minor axis, and the angle θ (Fig. 5). Our results relate to the time dependence of these quantities for different shear rates and quench depths. Table I summarizes all the runs performed in direction A and Table II all the runs in direction B. Note that the shear rates in Table II are reported for the outer cell. There is an uncertainty of 6% for these shear rates as mentioned in Sec. II C.

TABLE I. Summary of runs in direction A.

Run	ΔT (mK)	S (sec^{-1})	$S\tau$
A	0.8	0	0
B	0.8	0.035	0.080
C	0.8	0.087	0.198
D	0.8	0.35	0.797
E	1.8	0	0
F	1.8	0.035	0.017
G	1.8	0.087	0.043
H	1.8	0.35	0.172

TABLE II. Summary of runs in direction B.

Run	ΔT (MK)	S ($\sec^{-1}$)	$S\tau$
I	3.5	0	0
J	3.5	0.035	0.005
K	3.5	0.087	0.012
L	3.5	0.175	0.024
M	3.5	0.35	0.049
N	2.2	0	0
O	2.2	0.035	0.012
P	2.2	0.087	0.029
Q	2.2	0	0
R	2.2	0.175	0.059
S	2.2	0.35	0.117
T	2.2	0.875	0.294
U	2.2	0	0

B. Direction A

In this direction, there is a velocity gradient in a plane perpendicular to the laser beam [Fig. 4(a)]. The lengths of the major axis and minor axis are called k_a^m and k_b^m, respectively. Figures 6(a) and 6(b) show the time dependence of k_a and k_b for the quench of $\Delta T=0.8$ and 1.8 mK, respectively. In both Fig. 6(a) and Fig. 6(b), it can be seen that there are not data points for k_b^m after a certain time. This is due to the fact that the scattered intensities in this direction (end of the ellipse) disappear sometime after the quench and it is impossible to determine k_b^m. This phenomenon is shown in Fig. 5(b). Here we summarize the results of Figs. 6(a) and 6(b): (1) k_b^m disappears after a certain time; (2) k_a^m, at a fixed time, is smaller with higher shear rate and is not sensitive to the quench depth within experimental error [see Fig. 6(b)]; and (3) k_a^m follows a power law with a slope close to -1 at late times.

We also looked at the time dependence of the angle θ. Figure 7 represents the time dependence of $\tan(\theta)$ for two different quenches and for different rates. The main results are (1) at very low shear, the angle θ starts at around 45° and with time decreases toward zero; (2) $\tan(\theta)$ follows a power law with a slope close to -1 at late times; and (3) there is no systematic dependence of the angle θ on the quench depth within the experimental uncertainties.

C. Direction B

In this direction, there is no velocity gradient in the plane perpendicular to the laser beam. However, planes

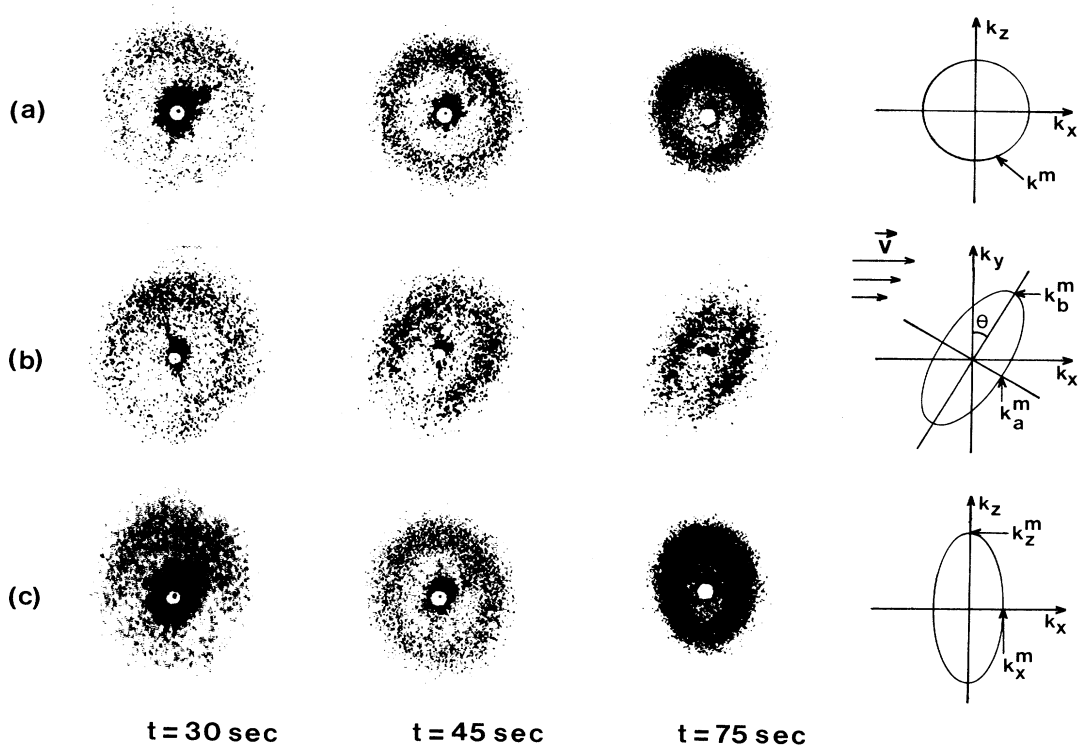

FIG. 5. Scattering pattern and definition of scattering parameters for spinodal decomposition under shear after a thermal quench of $\Delta T=1.5$ mK in the directions A and B at different times. (a) $S=0$ in direction B; (b) $S=0.035$ $\sec^{-1}$ in direction A and (c) $S=0.035$ $\sec^{-1}$ in direction B.

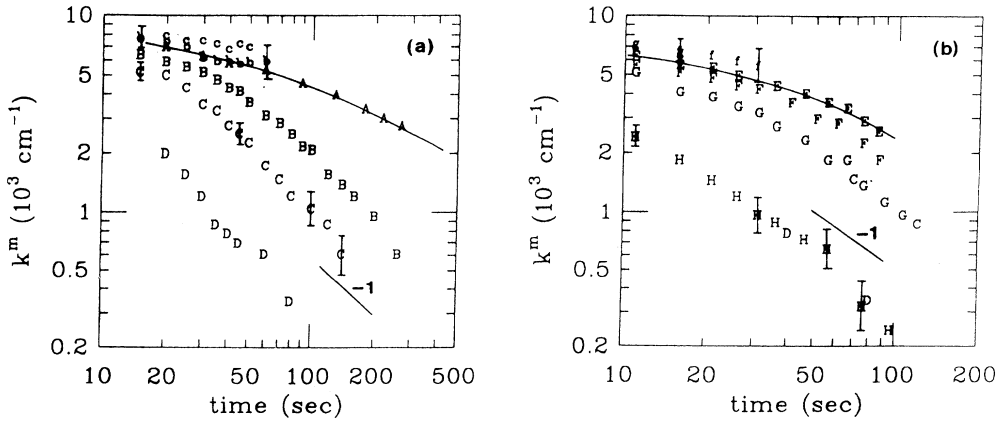

FIG. 6. Time dependence of k_a^m and k_b^m in direction A for different shear rates for a thermal quench of (a) $\Delta T=0.8$ mK and (b) $\Delta T=1.8$ mK. Small letters correspond to k_b^m and capital letters to k_a^m. The solid line corresponds to $S=0$ (runs A and E). See Table I for the meanings of the letters. In (b), the points C and D ($\Delta T=0.8$ mK) are plotted for comparison.

perpendicular to the laser beam are moving with different velocities. Figure 5(c) shows the scattering pattern in this direction for a typical quench of 1.5 mK with $S=0.035$ sec^{-1}. It is clear that there is a significant difference between the scattering patterns from direction A and direction B. In direction B, the angle θ is always zero and the intensities at the end of the ellipse never disappear. We will denote the length of the major axis and minor axis $k_z^m$and k_x^m, respectively. Figures 8(a) and 8(b) show their time dependences for different shears and quenches. Our findings in this direction are summarized as follows: (1) $\tan(\theta)=0$; (2) to within experimental error, k_z^m behaves like in the case of a thermal quench without shear; and (3) to within experimental error, k_x^m behaves like k_a^m.

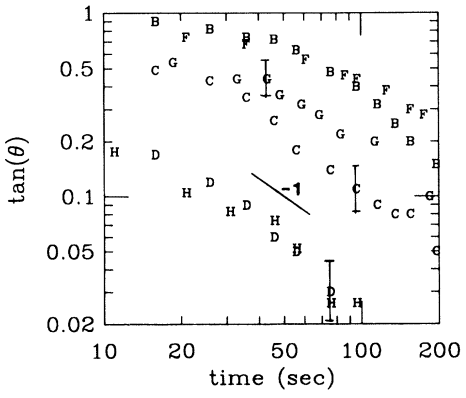

FIG. 7. Time dependence of the angle θ for different quenches and different shear rates in direction A. See Table I for the meanings of the letters.

D. Direction $A+B$ and multiple scattering

As mentioned above, k_x^m and k_a^m are measured in different runs. It is difficult to determine whether they are always equal because of different experimental situations. In order to compare the behaviors of k_a^m and k_x^m in greater detail, observation in both directions must be done at the same time. Figure 9 shows a typical result of the observations at these two directions at the same time for a 2.5-mK quench and $S=0.087$ sec^{-1}. Since the thickness of the sample along these two directions is not the same, the effect of multiple scattering is more important in direction A and a detailed comparison of the behaviors of k_a^m and k_x^m becomes difficult. Despite this, by measuring k_a^m an k_x^m for shallow quenches where multiple scattering is less important, we find that k_x^m and k_a^m are always roughly equal even for different shear rates.

One might think that the effect of multiple scattering can be calibrated by looking at quenches without shear, where the scattering in the two directions should be the same. Unfortunately, the scattering conditions change significantly when there is a shear flow and thus a proper calibration is not possible. However, we find that we have a better contrast when there is a shear flow (see Fig. 9).

IV. SIMULATION

In order to understand the meaning and possible interpretations of the above experimental observations, a numerical simulation was performed to generate scattering patterns of a simplified model of spinodal decomposition under shear flow. In this model, the growth process is assumed to have two stages which are shear dependent. In the early stage, the effect of shear is negligible and interconnected domains are formed, while at the late stage

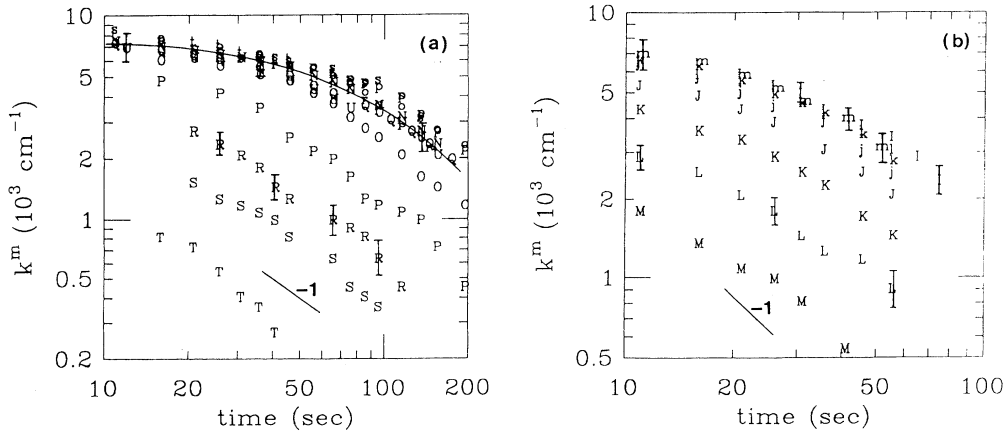

FIG. 8. Time dependence of k_x^m and k_z^m in direction B for different shear rates for a thermal quench of (a) $\Delta T=2.2$ mK and (b) $\Delta T=3.5$ mK. Small letters correspond to k_z^m and capital letters to k_x^m. The solid line corresponds to $S=0$ (runs I, N, Q, U). See Table II for the meanings of the letters.

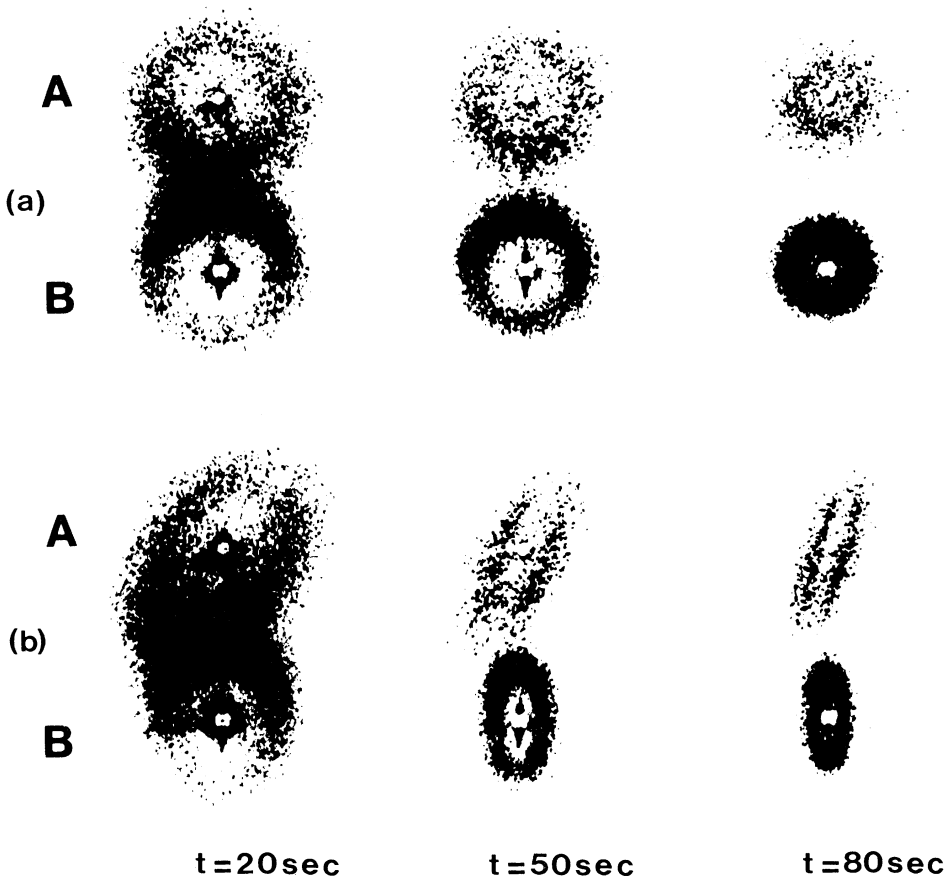

FIG. 9. Time evolution of the scattering patterns for the two experiments A and B, simultaneously with a quench of $\Delta T=2.5$ mK and with (a) $S=0$ and (b) $S=0.087$ sec^{-1}. The distance between the screen and the scattering volume in experiment B must be multiplied by 1.15 to be compared to those of experiment A.

only the effect of the flow is important. The justification of this simplification can be seen by comparing the different time scales of the problem. Thus in the simulation there is no growth mechanism; only the deformation effect of the shear flow is accounted for. The effect of surface tension is also neglected.

A. Theory

Consider the growth rate of the domains in a SD without shear. We are interested in how the growth rate changes with time. The growth rate $\Gamma(R)$ of an object of typical size $R(t)$ at time t can be defined as

$$\Gamma(R)=\frac{1}{R(t)}\frac{d}{dt}R(t) . \tag{1}$$

As time increases (after the Cahn linear regime[18] that is not experimentally attainable in binary fluids), effects of nonlinearities occur. This leads to an increase of the characteristic length with time:

$$R(t)\sim t^{\alpha} \tag{2}$$

where α varies from 0 (linear regime at very early times) to 1 (capillary growth at late times).[1,19] In reduced units (ξ^- for the length and τ^- for the time), all the experimental data for different quench depths lie on a universal curve which depends on two constants. The growth rate is thus given by

$$\Gamma(R)=\frac{\alpha}{t} , \tag{3}$$

so the growth rate decreases with time. With time, the distortion produced by the shear flow becomes greater than the growth of domains when $\Gamma(R)<S$ or equivalently $St>\alpha$.[9] Therefore there is a crossover in the region $St\sim 1$. The corresponding size R_0 depends both on the shear rate and on the quench depth. When $St\ll 1$, the effect of shear is negligible, and only the effect of growth is predominant. In the opposite case $St\gg 1$, the effect of deformation by shear is the most important.

Figure 10 shows the different regimes of this classification. In regime (1), the effect of shear is negligible; growth should not be affected. In regime (3), growth is controlled by the flow and should be strongly affected. However, in the crossover regime (2), the picture is less clear. We are mainly interested in regime (3), where most of our experimental observations were made. The simulation to be described below is also for this regime only. In this simulation, spinodal decomposition is not affected by shear up to a certain time and size $k_0(=2\pi/R_0)$ and then the effect of shear sets in suddenly, the crossover being assumed to be very sharp. We then only look at the deformation of the interconnected structures by shear flow and neglect the effects of surface tension.

B. Model and method

A spinodal structure is first generated on a $64\times64\times64$ array by using a method similar to that already used by Cahn.[18] This method essentially considers that the composition fluctuation $c(\mathbf{r})$ at a space point $\mathbf{r}$ is the superposition of random waves with different amplitudes and phases traveling in random directions but with the same modulus k_0 of wave number $\mathbf{k}$ as

$$c(\mathbf{r})=\sum_{|\mathbf{k}|=k_0} A\cos(\mathbf{k}\cdot\mathbf{r}+\phi_1)+B\sin(\mathbf{k}\cdot\mathbf{r}+\phi_2) \tag{4}$$

where A and B are random amplitudes and ϕ_1 and ϕ_2 are random phases. The composition fluctuations thus generated will assume continuous values between -1 and $+1$. However, in SD, there are only two equilibrium compositions separated by sharp interfaces. To simulate this bimodal distribution, we assign -1 to all fluctuations with values less than zero and $+1$ to all those greater than zero. Figure 11 shows the geometry of the simulations and Fig. 12(a) shows the bimodal composition fluctuations on the x-y plane.

The effect of shear is simulated by moving the concentration fluctuations with a shear motion and periodic boundary conditions: i.e., planes parallel to the plane $x-z$ are moved with different velocities depending on their distance from the y axis. Note that the direction of shear is in the y axis and motion of the composition fluctuations is in the x direction, as in the experiment. (The

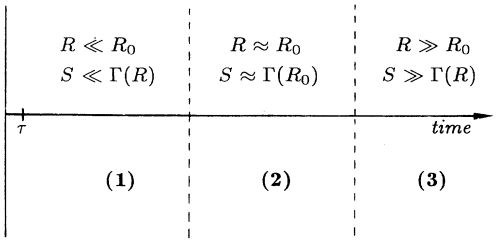

FIG. 10. Different regimes of growth and effect of shear (see test for notation).

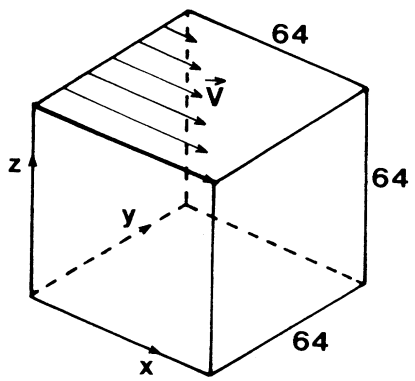

FIG. 11. Geometry of the sample ($64\times64\times64$ lattice) and of the shear flow in the simulation (one step).

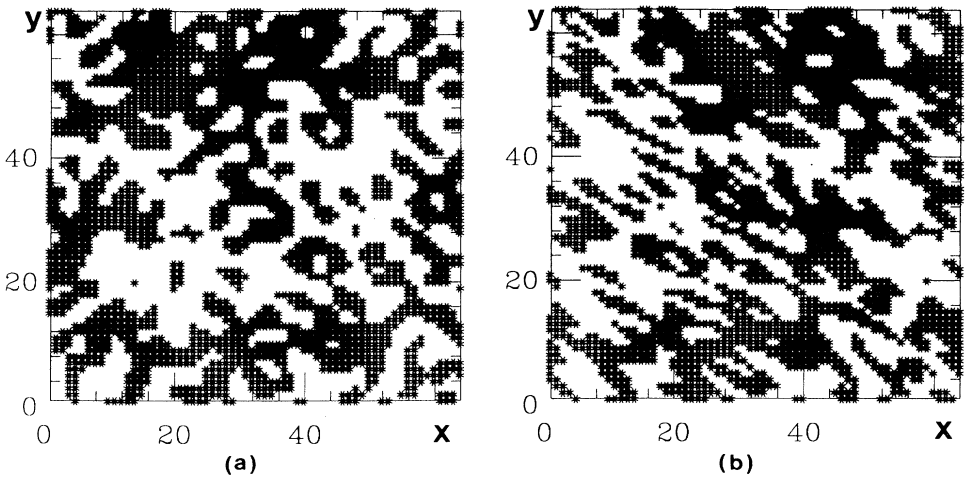

FIG. 12. 3D simulation of a spinodal decomposition pattern: section on a plane parallel to the x-y plane (a) before and (b) after a shear motion. Note that the velocity increases along the y axis toward the negative x.

periodic boundary conditions make a point which goes out of the sample come back from the other end.) In this simulation, the concentration fluctuations in a plane are moved relative to its neighboring planes one lattice point in one step, which is the unit of the discrete time. Since our sample is fixed to a $64\times64\times64$ lattice, the magnitude of the shear rate is changed by changing the step size. Thus we see that the step plays the role of both time and shear rate. Figure 12(a) shows the pattern of SD structure on an x-y plane generated by (4) before shear is applied and Fig. 12(b) gives the pattern after the shear motion. In these figures, the characteristic length $(2\pi/k_0)$ of the SD structure gives ten points of the lattice.

We are interested in how the light-scattering pattern from the structures generated by (4) is changed by shear. Since the scattered intensity (structure factor) is proportional to the square modulus of the Fourier transform of the composition fluctuations (when multiple scattering can be neglected,[20] scattering pattern from the sample is

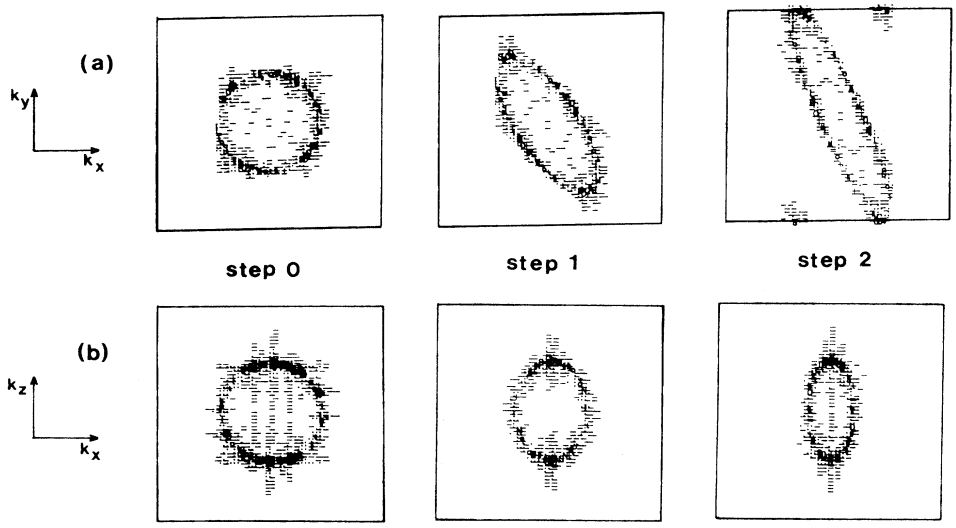

FIG. 13. Structure factor $S(k)$ obtained by Fourier transform from the simulation: (a) in the plane $k_z=0$ (direction A) and (b) in the plane $k_y=0$ (direction B) at different steps of the shearing motion.

calculated by first performing a three-dimensional (3D) fast Fourier transform (FFT) on the sample and then obtaining the power spectrum from this FFT. The power spectrum thus obtained is a 3D object. In order to compare it with our light-scattering experiments at small angles, we have to look at the cross section of the power spectrum on different orthogonal planes at the origin corresponding to $k_x=0$ (direction C), $k_y=0$ (direction B), or $k_z=0$ (direction A). This direction C would correspond to the situation where the laser beam is directed parallel to the flow; this experiment has not yet been carried out.

C. Results

Figure 13 shows the simulated scattering patterns at different steps for directions A and B for the first three steps. These are intensity plots with the darkest points corresponding to the highest intensities. Step 0 is for the structure generated by Eq. (4) and step 1 is for the structure obtained from step 0 after the shear motion described above has been applied once. Note that we have a mirror in direction A in our experiment and hence the experimental images are inverted. Comparing Figs. 13(a) and 13(b) with Figs. 5(b) and 5(c), it is clear that the simulation reproduces some remarkable features of the experiment. For example, there is a tilted ellipse in direction A and a vertical ellipse in direction B. If we take the step of simulation as being the time (at constant shear), we can compare the time dependence of k_a^m and k_b^m in direction A and k_x^m and k_z^m in direction B for both the simulation and the experiment.

Figure 14 shows the behavior of k_a^m and k_b^m in direction A. We will not give a graph for k_x^m and k_z^m here because in the simulation k_x^m and k_a^m are always equal and k_z^m is a constant equal to k_0. The angle $\tan(\theta)$ from the simulation is plotted in Fig. 15. It is clear that the behavior of k_a^m (k_x^m) and $\tan(\theta)$ from the simulation is very similar to that of the experiment, following a power law of about t^{-1} at late times. However, there are remarkable features in each of the directions of A and B that the simulation fails to reproduce. They are described in the following paragraphs.

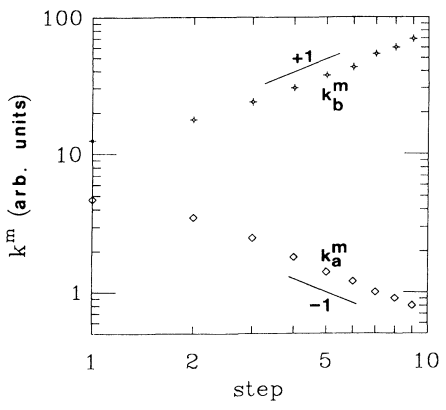

FIG. 14. Step dependence of k_a^m and k_b^m from simulation in direction A.

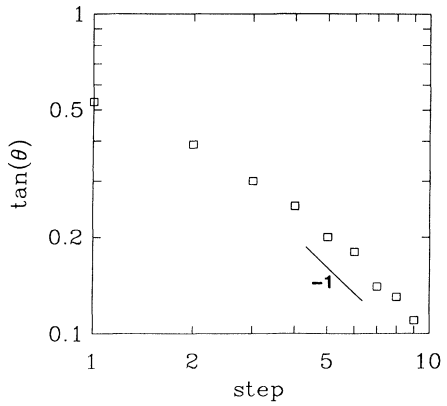

FIG. 15. Step dependence of $\tan(\theta)$ from simulation in direction A.

(1) In direction A: In the simulation the intensities of the major axis never disappear and the corresponding wave vector (k_b^m) keeps on increasing. In the experiments, the intensities at the ends of the ellipse disappear after a certain time and k_b^m is no longer well defined afterwards.

(2) In direction B: In the simulation, the vertical size of the ellipse k_z^m is not affected by shear and remains constant. In the experiments, although k_z^m seems not to be affected by shear, it is not constant.

These differences are probably due to the lack of growth mechanism in the simulation. This reinforces our assumption that hydrodynamics plays a very important role in this process. Although we have no experimental data to compare with in direction C, it is interesting to note that, in the simulation, the pattern remains a ring of radius k_0; shear has no effect at all in this direction.

V. DISCUSSIONS

It is clear that this simple simulation captures some essential features of our experimental observations. In order to compare our experimental results with that of the simulation quantitatively, we have to understand what one simulation step means in an actual experiment. As mentioned above, the step of the simulation plays the role of both time and shear rate. A similar parameter can be defined for the experimental results by expressing time in units of S^{-1}. We define a reduced dimensionless time h as $h=St$. In this reduced time unit, the effect of shear should be small when $h \ll 1$ and becomes important when $h \gg 1$, as shown in Sec. IV A. However, this dimensionless time h is not necessarily identical to a simulation step. They can differ by a multiplicative factor. This factor depends on the value of h at which the effect of shear becomes important in the actual experiment. In the simulation, it is clear that the effect of shear is impor-

tant even in one single step (Figs. 12 and 13). We will therefore determine this multiplicative factor by comparing the behavior of $\tan(\theta)$ from the simulation with that of the experiments. We have chosen $\tan(\theta)$ because $\tan(\theta)$ is a ratio of two lengths and is obviously independent of what length scale we are using. This is not the case when comparing quantities like k_a^m or k_b^m.

A. Behavior of $\tan(\theta)$

Figure 16(a) shows the step dependence of $\tan(\theta)$ from simulation. On the same log-log graph we have also plotted the experimental results for a quench of 0.8 mK and for $s=0.035$, 0.0875, and 0.35 $\sec^{-1}$ (Fig. 7) in reduced unit h. Note that the scale shown is that of the simulation step. Moreover we have marked the point at $h=10$ for the experimental data. When determining the marked position by horizontal translation of experimental data, we have assumed that the experiment and the simulation should give the same result at late times as we have argued above in Sec. IV A (there is a systematic deviation of experimental data from the simulation curve at early times). Nevertheless, it is remarkable that our simple model can reduce the data at different shear rates on one single curve. This multiplicative factor h_0 between h and one simulation step is determined by the value of h which corresponds to the first simulation step. This value is $h_0 \simeq 1$ in Fig. 16(a). We have also looked for the temperature dependence of h_0 by applying the same procedure to data from a different quench depth 1.8 mK. The 1.8-mK data are more scattered. However, they are compatible with the same value $h_0 \simeq 1$ [Fig. 16(b)].

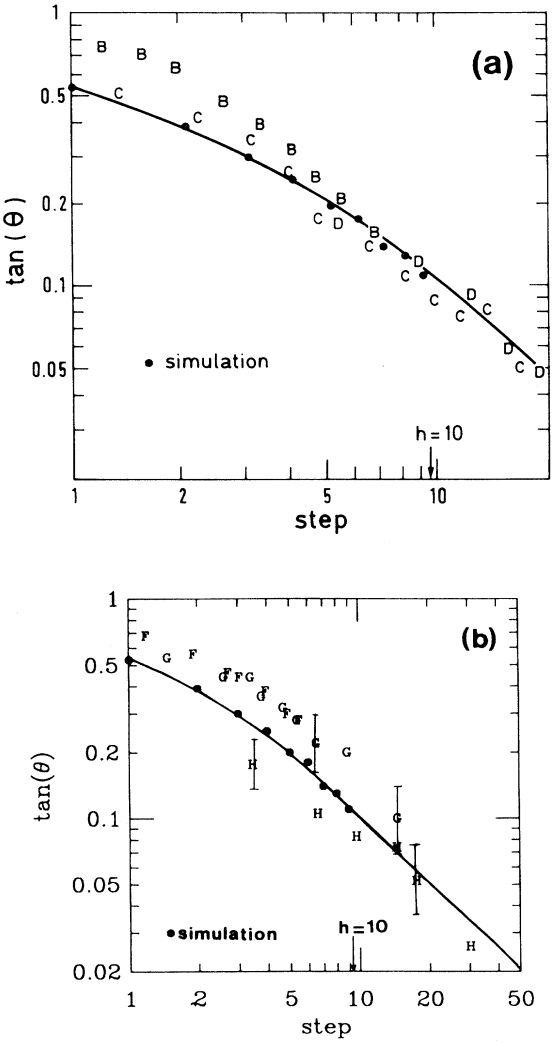

FIG. 16. Comparison of the step dependence of $\tan(\theta)$ (simulation curve) and of the $h(=St)$ dependence of $\tan(\theta)$ (experimental data). (a) $\Delta T=0.8$ mK; (b) $\Delta T=1.8$ mK. The letters correspond to Fig. 7 and Table I.

B. Behavior of k_a^m and k_x^m

To facilitate the comparison of our experimental observations with the simulation results, one remark about the experimental observations has to be made first: k_a^m and k_x^m are equal within experimental precision for different shear rates. This observation should not come as a surprise as it is seen in the simulation that k_x^m and k_a^m are always equal. In the following, we will therefore only discuss the behavior of k_a^m.

In the simulation, the size of k_a^m (or k_x^m) is governed by the initial size k_0 of Eq. (4), which is arbitrary and which will serve as length unit. Thus when comparing results from observations with that from the simulation, we can move the simulation curve vertically to fit our experimental data and determine k_0 from the fit. Figure 17 shows the time dependence of k_a^m, the same as in Fig. 6(a) but plotted in reduced time unit h together with the result of the simulation. Here we have used the same multiplica-

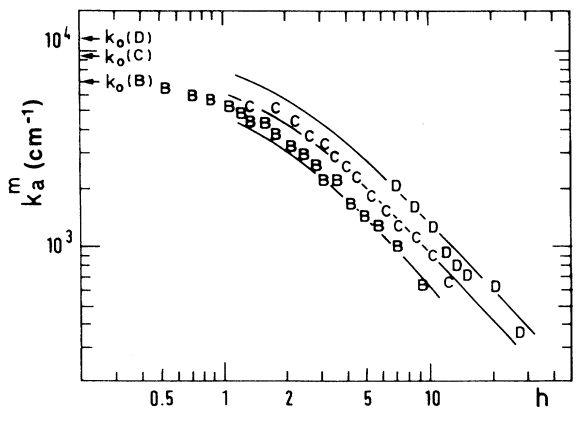

FIG. 17. Comparison of the h dependence of the wave vector k_a^m obtained with simulation and with experiment for a quench of $\Delta T=0.8$ mK and different shear rates. (See Table I for the meanings of the letters.)

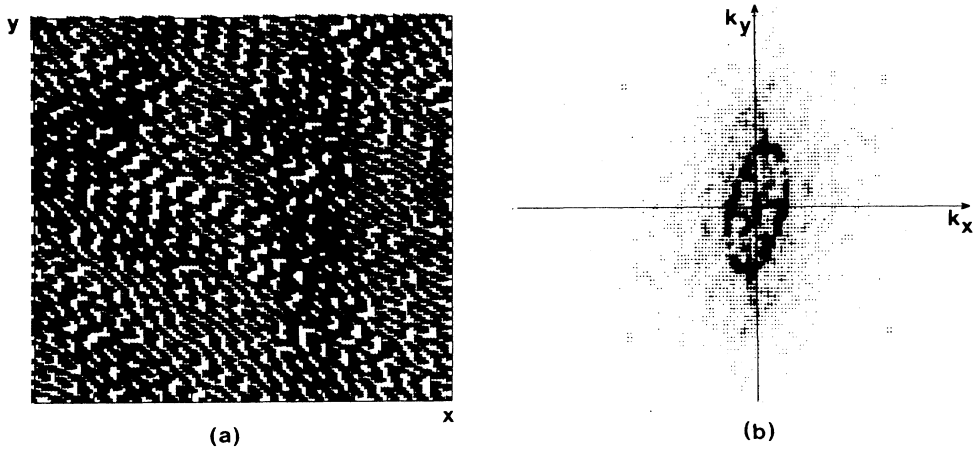

FIG. 18. (a) 2D spinodal composition parameter under shear and (b) its corresponding structure factor $S(k)$.

tive factor (h_0) between h and a step as obtained in Fig. 16. With the same assumption that the simulation and experimental results should agree at late times, in Fig. 17, three different simulation curves have been used (differential vertical movements) for a quench depth of 0.8 mK and for the three different shear rates.

An interesting feature of Fig. 17 is that the curve with the greater shear rate lies always higher than the curves with smaller shear rates. From these simulation curves, we have determined k_0 for $S=0.035$, 0.0875, and 0.35 $\sec^{-1}$ as $k_0=6900$, 9500 and 12 000 cm^{-1}, respectively. This dependence of k_0 on shear rate can be explained by the fact that at higher shear rates, smaller scales are being affected and thus the structures that the shear deforms have a higher k, as predicted in Sec. IV A.

Similar results are also obtained for k_a^m with another quench of 1.8 mK. The corresponding values are nearly the same as those obtained for a quench of 0.8 mK.

C. Behavior of k_b^m

Contrary to the success, to some degree, of our simple model, the simulation fails to reproduce the observed behavior of k_b^m, especially the disappearance of the intensity at the tip of the ellipse. This failure suggests that there are other important processes which occur in addition to the one that we have simulated. In the simulation, the wave vector k_b^m is increasing, so the corresponding length ($2\pi/k_b^m$) decreases. But the ultimate length scale is given by the thickness of the interfaces which is of order of some ξ^-.

In order to demonstrate this possible effect, we have

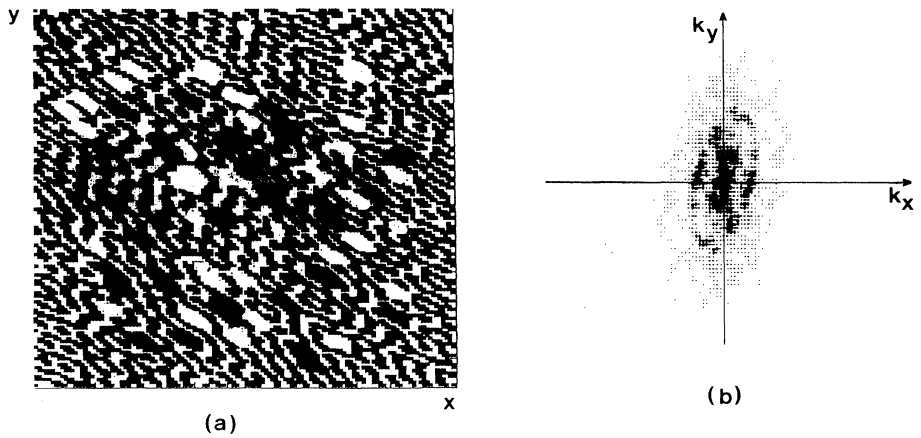

FIG. 19. (a) Same as Fig. 18(a) but with most of thin structures eliminated and (b) its corresponding structure factor $S(k)$.

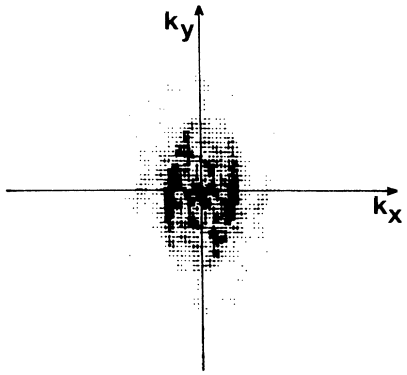

FIG. 20. Structure factor $S(k)$ of a blurred image of Fig. 18(a) produced by defocusing the video camers.

used a simple intuitive method on the SD structure in 2D. The reason for this choice is that it is difficult to simulate the effect of surface tension numerically in such a system and it will be seen that it is also difficult to apply our method in 3D. In this simple simulation, we have taken a SD pattern in 2D and performed a shear motion [Fig. 18(a)]. The 2D pattern of Fig. 18(a) will give an ellipse in the power spectrum as is shown in Fig. 18(b). This is accomplished by using an image processing system with input from a video camera. The effect of thickness of interfaces is simulated by eliminating thin structures "by hands" as shown in Fig. 19(a). Figure 19(b) shows the corresponding power spectrum of this modified pattern. It is clear that the intensity at the end of the ellipse has been lowered by this procedure. As a check, we have also deliberately defocused the video camera when processing the image of Fig. 18(a). In this process, the image is blurred and we lose all the thin structures. Figure 20 shows the structure scattering pattern obtained this way. We can see that this process of eliminating thin structures in a 2D SD pattern reproduces the essential features of our experiment in direction A.

D. Behavior of k_z^m

As for k_b^m, our simple simulation fails to reproduce the observed behavior of k_z^m. This is probably due to the fact that there is no growth in the simulation. The only observation in common in the simulation and the experiment is that k_z^m is found to be insensitive to the action of shear. Hence, the experimental time dependence of k_z^m is not affected by the deformation produced by the shear as in the case of k_a^m, k_b^m and k_x^m. However, although the surface tension is small, it is nonzero; consequently, it is surprising that there is no coupling between shear and flow in the z direction.

E. Comparison with theory: summary

To our knowledge, there are only two theories dealing with SD under shear. The first is due to Imaeda *et al.*[10,11] and is devoted to a thermal quench from above T_c to below T_c (Fig. 1) corresponding to the high shear condition ($S\tau_\xi \gg 1$). Rather surprisingly, the growth that was expected after such a quench corresponds to a 2D growth in layers *perpendicular to the flow.* This is different with our situation (weak shear) where one observes a growth in planes *nearly perpendicular to the shear.*

The second theory is more closely related to our experiment. It is due to Onuki[12] and corresponds to a quench into the weak-shear regime (region II of Fig. 1, $S\tau_\xi \ll 1$). Here the interest was in the steady state that ultimately occurs when growth is balanced by shear effects. Gravity was not accounted for. In this steady state it is assumed that the phase-separating fluid under shear is composed of isolated elongated droplets. These droplets have to break up into smaller droplets which are weakly anisotropic with respect to the flow direction (sizes $R_\parallel$ and $R_\perp$), respectively parallel and perpendicular to the flow). These lengths are always much larger than the interface thickness, which in $3D$ is of order of the correlation length. The typical size of these small droplets results from the balance between the growth velocity ($\sim\sigma/\eta$) and a deformation velocity ($\sim RS$). The steady state corresponds to

$$R_\parallel \simeq 3R_\perp \sim \frac{\sigma}{\eta S} \ . \tag{5}$$

Our case differs from that of Onuki in the sense that in our experiment, we have not yet reached a steady state. (The attainment of such a steady state is in practice hampered by weak remaining gravity flows that becomes important at late times.) What we are looking at is rather how the growth process is modified by a weak-shear flow. And as in Onuki's theory, the shear is so weak that it is not expected to act at the level of the interface (case $S\tau_\xi \ll 1$). Our main findings are summarized as follows.

1. No action of shear is seen until the growth rate is smaller than the deformation rate ($St < 1$), i.e., the domains are isotropic and grow as [see Eq. (2)]

$$R \sim \frac{\sigma}{\eta} t^\alpha \quad \text{with } \alpha = 0.3-1 \ .$$

2. In the regime $St > 1$, the growth is seen or proceed apparently independently according to the three axes.

(i) Along the flow direction (x), the growth is governed by flow and corresponds to the size $R_\parallel$ of Onuki's theory. The dependence with shear with the typical length that results does not correspond to Eq. (5), but rather to

$$R_\parallel \sim S^x t \ ,$$

with x of order of unity.

(ii) Along the shear direction (y), the correlation between the interfaces of domains is suppressed up to the interface thickness, of order of the correlation length ξ^-:

$$R_{\perp,y} \sim \xi^- \ .$$

(iii) In the direction perpendicular to the shear and to

the flow (z), growth proceeds as if there were no shear flow:

$$R_{\perp,z} \sim \frac{\sigma}{\eta} t \ .$$

VI. CONCLUDING REMARKS

The independence of growth in the directions x and z can be related to the near-zero value of the surface tension in the interconnected pattern. This is supported by the close correspondence between the experiment and the numerical simulation (where there are no surface tension effects) along these two directions. In the shear direction (y), where experiment and simulation are different, correlations between interfaces are lost, up to the scale of the correlation length. The image of growth that emerges is therefore that of an anisotropic interconnected pattern that grows in layers nearly perpendicular to the shear. We interpret all these results as if the growth through the action of shear had acquired a two-dimensional character. A scattering experiment with the laser beam in the direction of flow is actually being set up to definitely check this point.

*Present address: Institute of Physics, Academia Sinica, Nankan, Taipei, Taiwan 11529.

[1]E. D. Siggia, Phys. Rev. A **20**, 595 (1979).

[2]T. Benda, P. Alpern, and P. Leiderer, Phys. Rev. B **26**, 1450 (1982).

[3]C. K. Chan and W. I. Goldberg, Phys. Rev. Lett. **58**, 674 (1987).

[4]See, e.g., H. E. Stanley, *Introduction to Phase Transitions and Critical Phenomena* (Clarendon, Oxford, 1971).

[5]A. Onuki, K. Yamasaki, and K. Kawasaki, Ann. Phys. (N.Y.) **131**, 217 (1981), and references therein; D. Beysens, M. Gbadamassi, and B. Moncef-Bouanz, Phys. Rev. A **28**, 2491 (1983), and references therein.

[6]A. Onuki and K. Kawasaki, Physica A **111**, 607 (1982); D. Beysens and M. Gbadamassi, Phys. Rev. Lett. **47**, 846 (1981); Y. C. Chou and W. I. Goldberg, *ibid.* **47**, 1155 (1981); D. Beysens, R. Gastaud, and F. Decruppe, Phys. Rev. A **30**, 1145 (1984).

[7]D. Beysens and F. Perrot, J. Phys. (Paris) Lett. **45**, L31 (1984).

[8]C. K. Chan, F. Perrot, and D. Beysens, Phys. Rev. Lett. **61**, 412 (1988).

[9]F. Perrot, C. K. Chan, and D. Beysens, Europhys. Lett. **9**, 65 (1989).

[10]T. Imaeda, A. Onuki, and K. Kawasaki, Prog. Theor. Phys. **71**, 16 (1984).

[11]T. Imaeda and K. Kawasaki, Prog. Theor. Phys. **73**, 559 (1985).

[12]A. Onuki, Phys. Rev. A **34**, 3528 (1986).

[13]S. Chandrasekhar, *Hydrodynamic and Hydromagnetic Stability* (Oxford University Press, Oxford, 1961).

[14]D. Beysens, A. Bourgou, and G. Paladin, Phys. Rev. A **30**, 2866 (1984), and references therin.

[15]See, e.g., R. H. Cohn and D. T. Jacobs, J. Chem. Phys. **80**, 856 (1984).

[16]C. K. Chan, Rev. Sci. Instrum. **59**, 1001 (1988).

[17]P. Guenoun, R. Gastaud, F. Perrot, and D. Beysens, Phys. Rev. A **36**, 4876 (1987).

[18]J. W. Cahn, J. Chem. Phys. **42**, 93 (1965).

[19]J. S. Langer, M. Bar-On, and H. D. Miller, Phys. Rev. A **11**, 1417 (1975); K. Kawasaki and T. Ohta, Physica A **118**, 175 (1983). For a recent review, see, e.g., H. Furukawa, Adv. Phys. **34**, 703 (1985).

[20]See, e.g., B. Chu, *Laser Light Scattering* (Academic, New York, 1974).